

Enhancing nitrate reduction to ammonia by synergistic and interface coupling effects of binary metal sites

Qiao Gou ^{a,1}, Yini Mao ^{a,1}, Shengmei Lv ^a, Fenglin Gou ^a, Yimin Jiang ^a, Wei Shen ^a, Ming Li ^a, Yun Wang ^{b,*}, Rongxing He ^{a,*}

^a Key Laboratory of Luminescence Analysis and Molecular Sensing (Southwest University), Ministry of Education College of Chemistry and Chemical Engineering, Southwest University, Chongqing 400715, PR China

^b Centre for Catalysis and Clean Energy, School of Environment & Science, Griffith University, Australia



ARTICLE INFO

Keywords:
Synergistic
Interface coupling
Nitrate reduction
Binary metal sites
Ammonia

ABSTRACT

Electrochemical nitrate reduction to ammonia (NRA) provides a sustainable and energy-efficient technical solution. Herein, we reported a synergistic bimetallic oxides $\text{Fe}_3\text{O}_4/\text{SnO}_2/\text{NF}$ with heterointerfaces for efficient NRA. The interfacial charge transfer at the heterointerfaces between Fe_3O_4 and SnO_2 improves the adsorption and activation of nitrate and intermediates, and strongly inhibits the production of by-products (NO_2) and the occurrence of HER. Experimental and theoretical results verify that the Fe sites activate NO_3^- , while the Sn sites dissociate H_2O molecules to provide necessary $^*\text{H}$ for the Fe sites to reduce NO_3^- . Benefiting from the interfacial engineering and synergistic effect of Fe and Sn, $\text{Fe}_3\text{O}_4/\text{SnO}_2/\text{NF}$ exhibits excellent NRA performance (NH_3 Faradaic efficiency: 98.78%, NH_3 yield: $0.2584 \text{ mmol h}^{-1} \text{ cm}^{-2}$, NH_3 selectivity: 98.85%, and NO_3^- conversion: 90.19%), which is significantly superior to $\text{Fe}_3\text{O}_4/\text{NF}$ and SnO_2/NF . This work provides a powerful approach for constructing synergistic heterojunction and contribute a promising strategy for designing efficient electrocatalysts.

1. Introduction

Ammonia (NH_3) is one of the most produced chemicals in the world, accounting for 5% of the market value of chemical products, and 80% of ammonia is used for producing agricultural fertilizers. Besides, NH_3 is a feedstock for medicine, refrigerant, and fabrics. Currently, thermochemical methods for NH_3 synthesis (the Haber-Bosch process) rely on high temperature and high pressure to drive chemical reactions. Consumption of natural gas and emissions of CO_2 lead to serious energy and environmental problems [1–3]. Electrochemical reduction of nitrogen (N_2) to synthesize NH_3 (NRR) is a promising alternative to the energy intensive Hubble-Bosch process. However, NRR typically results in relatively low NH_3 yield and NH_3 Faraday efficiency (FE) due to its extremely low N_2 solubility, ultra-stable $\text{N}\equiv\text{N}$ bond, and severe competitive hydrogen evolution reaction (HER) [4–6].

The electrochemical nitrate reduction to ammonia (NRA), $\text{NO}_3^- + 9 \text{H}^+ + 8\text{e}^- \rightarrow \text{NH}_3 + 3 \text{H}_2\text{O}$, is another candidate pathway for ammonia synthesis [1,7,8]. Nitrate is one of the main environmental pollutants,

and widely exists in industrial wastewater and domestic sewage [9]. NRA not only achieves the production of ammonia, but also the environmental remediation. Due to the significantly lower dissociation energy of the N-O bond (204 kJ mol^{-1}) of the adsorbed reactant NO_3^- compared to the $\text{N}\equiv\text{N}$ bond (941 kJ mol^{-1}) of N_2 , NRA is more prone to occur than NRR [10–12]. Moreover, NO_3^- can be adsorbed to the surface of catalysts more easily than N_2 under ambient conditions. However, the difficulty of charge transfer to the π -orbital of nitrate results in sluggish reaction kinetics in the NRA process [13,14]. Therefore, there is an urgent need to develop powerful catalysts to promote the conversion of NO_3^- to NH_3 while inhibiting by-products and competing HER [15,16].

NRA involves not only nitrate adsorption but also a hydrogenation process that is heavily dependent on water splitting [17–21]. $^*\text{H}$ produced by dissociating water is captured by the intermediates of NO_3^- to NH_3 , facilitating the hydrogenation process of NO_3^- reduction. With the advantages of non-toxicity, wide availability, and low cost, iron-based catalysts have become a promising material for electrochemical NRA in recent years. The unfilled 3d orbital of iron can easily pair with the

* Corresponding authors.

E-mail addresses: yun.wang@griffith.edu.au (Y. Wang), herx@swu.edu.cn (R. He).

¹ These authors contributed equally to this work.

extranuclear electrons of O in the N-O bond of nitrate, thus favoring the adsorption of NO_3^- [22]. However, the Fe_3O_4 surface lacks inherent active sites for the adsorption of $^*\text{H}$ [23,24], which is unfavorable for the hydrogenation of nitrate reduction. It has been shown that SnO_2 can play a role adsorbing $^*\text{OH}$ during water splitting, which promotes the formation of $^*\text{H}$ [25,26]. The moderate adsorption strength of H on catalyst surface facilitates ammonia formation and also inhibits H-H dimerization [18,27]. Interestingly, the heterointerfaces of catalyst can integrate the functions of multiple components and modulate the electronic structure of each component to induce charge redistribution [28]. It is reported that the interfacial engineering can effectively boost the NRA efficiency by optimizing the adsorption strength of nitrate, increasing electron transfer rate and exposing more active sites [29–32]. Therefore, designing and synthesizing iron-based/ SnO_2 catalysts based on interfacial engineering to achieve division of labor among various components and synergistically improve the performance of NRA is a promising strategy.

Herein, $\text{Fe}_3\text{O}_4/\text{SnO}_2/\text{NF}$ with heterointerfaces was synthesized by a combination of hydrothermal and calcination methods. $\text{Fe}_3\text{O}_4/\text{SnO}_2/\text{NF}$ obtains an outstanding electrocatalytic NRA performance with FE of 98.78%, NH_3 yield of $0.2548 \text{ mmol h}^{-1} \text{ cm}^{-2}$, NH_3 selectivity of 98.85% and NO_3^- conversion of 90.19% at -0.49 V , which are significantly better than that of the contrast samples $\text{Fe}_3\text{O}_4/\text{NF}$ and SnO_2/NF . Experimental and theoretical results show that charge redistribution at heterointerfaces modulates the electronic structures of Fe_3O_4 and SnO_2 and thus enhances the adsorption of NO_3^- and intermediates. Of particular interest is that during catalytic processes, the Fe atom is acted as the active site for adsorbing nitrate, while Sn is the active site for dissociating water molecules to generate H. This synergistic effect of Fe and Sn sites on the heterointerfaces promotes the adsorption and activation of NO_3^- and inhibits the occurrence of HER, resulting in the excellent NRA performance of the $\text{Fe}_3\text{O}_4/\text{SnO}_2/\text{NF}$ catalyst.

2. Experimental section

2.1. Synthesis of $\text{Fe}_3\text{O}_4/\text{SnO}_2/\text{NF}$ with heterointerfaces

The $\text{Fe}_3\text{O}_4/\text{SnO}_2/\text{NF}$ catalyst with heterointerfaces was fabricated using a combination of hydrothermal process and heat-treatment. Firstly, a piece of nickel foam (NF) was ultrasonically cleaned in HCl, ethanol solution and deionized (DI) water for 10 min, separately. Subsequently, the NF was immersed in a 50 mL Teflon-lined autoclave with a solution consisting of 1 mmol $\text{Fe}(\text{NO}_3)_3 \cdot 9 \text{ H}_2\text{O}$, 1 mmol $\text{SnCl}_2 \cdot 2 \text{ H}_2\text{O}$, 6 mmol $\text{CO}(\text{NH}_2)_2$, and DI water. After that, the autoclave was held for eight hours at 120°C . The precursor was repeatedly cleaned using ethanol and water in turn, and it was then vacuum-dried for 12 h at 60°C . Lastly, the precursor was annealed for 2 h at 300°C in Ar to obtain $\text{Fe}_2\text{O}_3/\text{SnO}_2/\text{NF}$, followed by calcination for 2 h in a H_2/Ar (10:90) atmosphere. The catalyst obtained was named $\text{Fe}_3\text{O}_4/\text{SnO}_2/\text{NF}$. The pristine $\text{Fe}_3\text{O}_4/\text{NF}$ catalyst was fabricated by the same method without adding $\text{SnCl}_2 \cdot 2 \text{ H}_2\text{O}$. The synthesis of SnO_2/NF catalyst was described in the [Supplemental materials](#).

2.2. Characterizations

The morphology of samples was characterized by scanning electron microscopy (SEM, FlexSEM 1000), high-resolution transmission electron microscopy (HRTEM), and transmission electron microscopy (TEM, FEI Tecnai F20). X-ray diffraction (XRD) was carried out on a Bruker D2 PHASER system using Cu K α radiation. ^1H NMR spectra were acquired by a Bruker AV600 spectrometer (Switzerland). Chemical state information was obtained by X-ray photoelectron spectroscopy (XPS) on a Thermo Scientific K-Alpha spectrometer. The ultraviolet-visible (UV-vis) absorbance was obtained on TU-1901 (Beijing General Analysis Instrument Co., Ltd.). The X-ray absorption fine structure spectra (Fe K-edge) were collected at 1W1B station in Beijing Synchrotron

Radiation Facility (BSRF). The in situ Raman spectra were obtained by an inVia laser micro Raman spectrometer (Renishaw, UK).

2.3. Electrochemical measurements

Benefiting from the abundant heterointerfaces, $\text{Fe}_3\text{O}_4/\text{SnO}_2/\text{NF}$ was employed as electrocatalysts for NRA. Electrochemical measurements were carried out on a CHI 660E electrochemical workstation with an H-type electrolytic cell at ambient condition. The cathode and anode chambers of the electrolytic cell were separated by a Nafion 211 membrane. The prepared $\text{Fe}_3\text{O}_4/\text{SnO}_2/\text{NF}$ electrocatalyst, Pt wire, and Ag/AgCl electrode were assembled into a three-electrode system for the electrocatalytic study. The anode electrolyte was 0.5 M K_2SO_4 solution (20 mL), while the cathode was 0.5 M $\text{K}_2\text{SO}_4 + 200 \text{ ppm KNO}_3$ -N solution (20 mL). The linear sweep voltammetry (LSV) curves were recorded at a scan rate of 5 mV s^{-1} . Furthermore, the chronoamperometric measurements ($i-t$) were performed at different potentials for 1 h under a stirring speed of 500 rpm. Potential versus RHE was calculated using the formula $E_{\text{RHE}} = E_{\text{Ag}/\text{AgCl}} + 0.197 + 0.0591 \times \text{pH}$. Electrochemical impedance spectroscopy (EIS) was recorded with a frequency range from 10 kHz to 0.01 Hz and an amplitude of 5 mV at -0.49 V . The electrochemically active surface area (ECSA) was estimated by measuring the double-layer capacitance (C_{dl}) via the CV test at scan rates of $6-16 \text{ mV s}^{-1}$. The detailed analytical methods for the determination of products NRA are supplied in the [Supporting Information](#).

2.4. Calculation details

First-principles calculations were performed based on the density functional theory (DFT) implemented in the Vienna ab initio simulation package (VASP) [33]. The projector-augmented wave (PAW) approach [34] with a cutoff energy of 520 eV, and dispersion corrections were calculated using the DFT-D3 method of Grimme [35]. To account for the strong on-site Coulombic interactions from the localization of the Fe 3d orbitals, an effective U value of 5.3 eV was applied using the DFT+U method by Dudarev et al. [36]. The Fe_3O_4 (220) and SnO_2 (110) surfaces were selected as the model for theoretical calculations. The vacuum layer in the z-axis direction was set at 15 Å. The Brillouin zone was sampled by $2 \times 2 \times 1$ special k-points [37]. The force convergence thresholds were $0.02 \text{ eV}\text{\AA}^{-1}$ and the total energy less than 10^{-5} eV , respectively. The associated free energy is determined from Eq. (1):

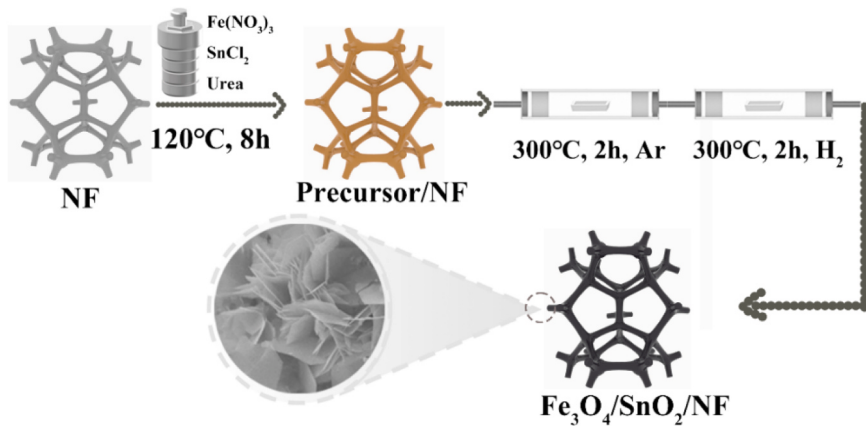
$$\Delta G = \Delta E + \Delta E_{ZPE} - T\Delta S \quad (1)$$

where ΔE is the total energy change before and after intermediate adsorbed, ΔE_{ZPE} is the change of zero-point energy, and ΔS is the entropy change between the adsorbed state and gas phase. The energy of charged NO_3^- is not calculated directly; instead, gaseous HNO_3 is used as a reference [38–40].

3. Results and discussion

3.1. Characterization of catalysts

$\text{Fe}_3\text{O}_4/\text{SnO}_2/\text{NF}$ was fabricated using a combination of hydrothermal process and heat-treatment ([Scheme 1](#)). SEM and TEM were used to investigate micromorphology of the samples. The SEM images of $\text{Fe}_3\text{O}_4/\text{SnO}_2/\text{NF}$ ([Fig. 1a](#) and b) clearly show that the 2D nanosheets are completely grown on the NF. The morphology of the control samples $\text{Fe}_3\text{O}_4/\text{NF}$ and SnO_2/NF are shown in [Figs. S1 and S2](#). The TEM images further confirm the nanosheet morphology of $\text{Fe}_3\text{O}_4/\text{SnO}_2/\text{NF}$ ([Fig. 1c](#) and d), and clearly demonstrates the heterointerfaces of $\text{Fe}_3\text{O}_4/\text{SnO}_2/\text{NF}$ ([Fig. 1e](#)). Furthermore, the magnified TEM image of $\text{Fe}_3\text{O}_4/\text{SnO}_2/\text{NF}$ ([Fig. 1f](#)) exposes the lattice fringe distances of 0.30 nm and 0.33 nm, indexed to the (220) and (110) planes of Fe_3O_4 and SnO_2 , respectively, certifying again the successful formation of $\text{Fe}_3\text{O}_4/\text{SnO}_2/\text{NF}$ with



Scheme 1. A simplified illustration of the entire preparation procedure for the $\text{Fe}_3\text{O}_4/\text{SnO}_2/\text{NF}$.

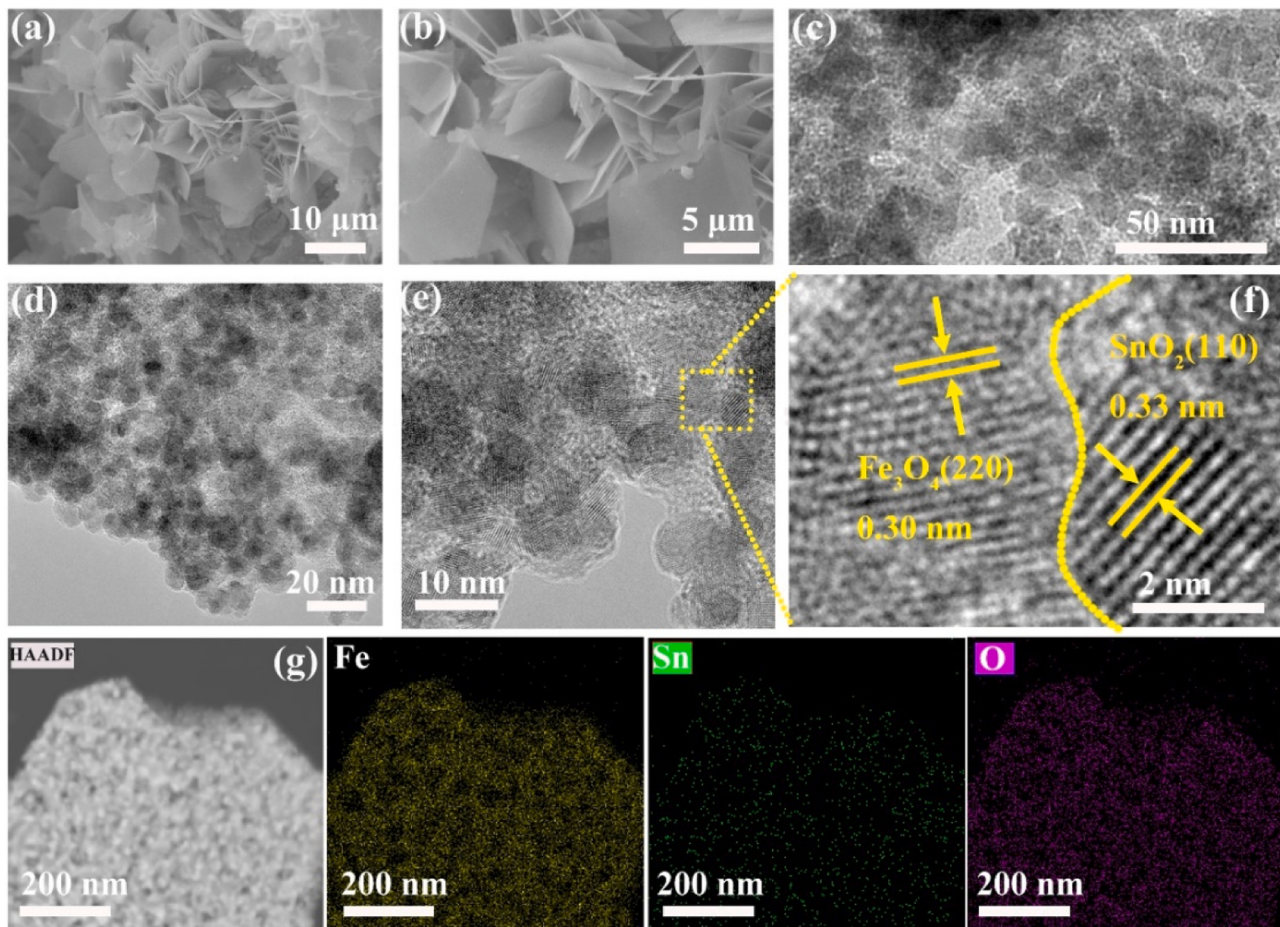


Fig. 1. (a, b) Scanning electron microscope at different magnifications and (c, d) HRTEM images of $\text{Fe}_3\text{O}_4/\text{SnO}_2/\text{NF}$. (e) TEM image of $\text{Fe}_3\text{O}_4/\text{SnO}_2/\text{NF}$ heterointerfaces. (f) Magnified TEM image of $\text{Fe}_3\text{O}_4/\text{SnO}_2/\text{NF}$ heterointerfaces. (g) TEM-EDX elemental mapping for Fe, Sn, and O.

heterointerfaces. Energy dispersive X-ray (EDX) mapping images (Fig. 1 g) show that Fe, Sn, and O disperse uniformly in the $\text{Fe}_3\text{O}_4/\text{SnO}_2/\text{NF}$ catalyst.

During the synthesis, the samples were obtained after two steps of calcination. The sample obtained after the first calcination step was $\text{Fe}_2\text{O}_3/\text{SnO}_2/\text{NF}$ (Fig. S3a). Then, using the H_2/Ar atmosphere to reduce Fe_2O_3 to Fe_3O_4 , and the EPR experiments show that this process produces almost no oxygen vacancies on the catalyst surface (Fig. S3b). The crystal structure of $\text{Fe}_3\text{O}_4/\text{SnO}_2/\text{NF}$ was investigated by XRD. As shown in Fig. 2a, the XRD diffraction peaks are well ascribed to cubic Fe_3O_4

(PDF#89-4319) and tetragonal SnO_2 (PDF#41-1445). Moreover, the weak peaks located at 44.5° , 51.8° and 76.3° were attributed to (111), (200), and (220) planes of NF substrate (PDF#04-0850). The $\text{Fe}_3\text{O}_4/\text{NF}$ and SnO_2/NF were also synthesized successfully as the control samples (Fig. S4). As seen in Fig. 2b-d, XPS was used to examine elemental composition and surface chemical states of these materials. The survey spectra (Fig. 2b) of $\text{Fe}_3\text{O}_4/\text{SnO}_2/\text{NF}$ identify the presence of Ni, Fe, Sn and O. As shown in the XPS spectrum of Fe 2p in $\text{Fe}_3\text{O}_4/\text{SnO}_2/\text{NF}$ (Fig. 2c), the binding energies (BEs) at 711.57 and 724.98 eV can be ascribed to Fe^{2+} , and the other peaks at 714.90 and 729.59 eV are

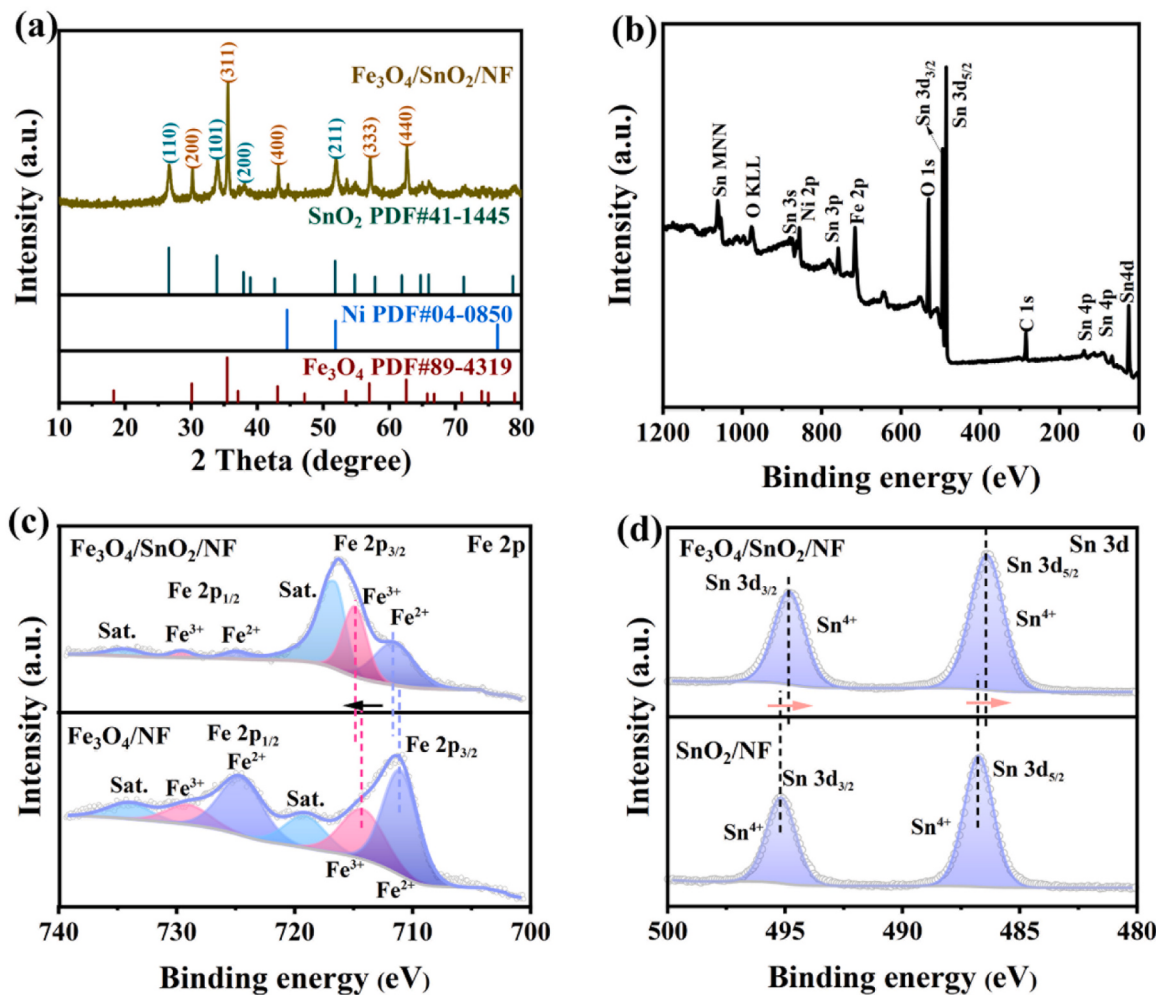


Fig. 2. (a) XRD pattern of $\text{Fe}_3\text{O}_4/\text{SnO}_2/\text{NF}$. (b) XPS survey spectra of $\text{Fe}_3\text{O}_4/\text{SnO}_2/\text{NF}$. (c, d) XPS spectra of Fe 2p and Sn 3d for $\text{Fe}_3\text{O}_4/\text{SnO}_2/\text{NF}$.

attributed to Fe^{3+} . The BEs located at 716.62 and 734.56 eV are assigned to the satellite peaks (Sat.) [41,42]. The Sn 3d spectrum of $\text{Fe}_3\text{O}_4/\text{SnO}_2/\text{NF}$ can be fitted into two peaks at 486.39 and 494.82 eV, belonging to $\text{Sn } 3\text{d}_{5/2}$ and $\text{Sn } 3\text{d}_{3/2}$, respectively [42–44], which suggests that the Sn in $\text{Fe}_3\text{O}_4/\text{SnO}_2/\text{NF}$ is Sn^{4+} . As compared to $\text{Fe}_3\text{O}_4/\text{NF}$ and SnO_2/NF , the XPS peaks of Fe^{2+} and Fe^{3+} in $\text{Fe}_3\text{O}_4/\text{SnO}_2/\text{NF}$ positively shift by 0.52 eV and 0.65 eV, respectively, while that of Sn^{4+} in $\text{Fe}_3\text{O}_4/\text{NF}$ negatively shifts by 0.36 eV. The phenomenon can be explained by the different Fermi levels of Fe_3O_4 and SnO_2 , resulting in the charge transfer from Fe_3O_4 to SnO_2 [45], which suggests that the formation of $\text{Fe}_3\text{O}_4/\text{SnO}_2/\text{NF}$ with heterointerfaces can modulate the electronic structure of Fe_3O_4 and SnO_2 , thereby modulating the adsorption behavior of reaction intermediates.

To further ascertain the fine structure of $\text{Fe}_3\text{O}_4/\text{SnO}_2/\text{NF}$ and the chemical state of Fe, the X-ray absorption near edge structure (XANES) and extended X-ray absorption fine structure (EXAFS) spectra were performed. Fig. 3a displays the Fe K-edge XANES of $\text{Fe}_3\text{O}_4/\text{SnO}_2/\text{NF}$, Fe_3O_4 , FeO , Fe_2O_3 , and Fe foil standard substances. The absorption edge of Fe K-edge in $\text{Fe}_3\text{O}_4/\text{SnO}_2/\text{NF}$ is between FeO and Fe_2O_3 , suggesting the oxidation state of Fe in the heterostructure is in the oxidation state between + 2 and + 3. Interestingly, the Fe K-edge absorption energy of $\text{Fe}_3\text{O}_4/\text{SnO}_2/\text{NF}$ after NRA is slightly negatively shifted compared with that of $\text{Fe}_3\text{O}_4/\text{SnO}_2/\text{NF}$ before NRA, which implies a slight decrease in the oxidation state of Fe. This result suggests that Fe species play a crucial role in the NRA process and may be the active site of NRA. The relevant Fe K-edge signal in k^3 -weighted EXAFS spectra was recovered in order to define the local coordination environment, particularly the Fe

local structure. As shown in Fig. 3b, the EXAFS spectrum shows that the distance of Fe-O for $\text{Fe}_3\text{O}_4/\text{SnO}_2/\text{NF}$ is 1.50 Å, while Fe-O for $\text{Fe}_3\text{O}_4/\text{NF}$ is 1.53 Å (Table S1). The fact that the bond distance of Fe-O is obviously shortened implies the Fe-O bond is stronger, further proving the significant electronic interaction between Fe_3O_4 and SnO_2 [46,47]. As shown in Fig. 3b, the EXAFS spectrum shows the presence of Fe-O bonds in the initial $\text{Fe}_3\text{O}_4/\text{SnO}_2/\text{NF}$. After NRA, the Fe-O bonds still exist in $\text{Fe}_3\text{O}_4/\text{SnO}_2/\text{NF}$. Furthermore, the Fe K-edge EXAFS $k^3\chi(k)$ oscillation curve of $\text{Fe}_3\text{O}_4/\text{SnO}_2/\text{NF}$ exhibits a similar frequency before and after the NRA testing (Fig. 3c). The result indicates that the catalyst still remains the structure of metal oxide and demonstrates the good stability of the catalyst.

3.2. Electrochemical performance

The electrocatalytic performance of $\text{Fe}_3\text{O}_4/\text{SnO}_2/\text{NF}$ was measured to evaluate the NRA catalytic activity. The linear scanning voltammetry curve (LSV) of catalysts were determined in 0.5 M K_2SO_4 + 200 ppm KNO_3 and blank electrolyte. It is worth noting that the current density of the $\text{Fe}_3\text{O}_4/\text{SnO}_2/\text{NF}$ in the nitrate can reach 114 mA cm^{-2} (Fig. 4a, orange line) is much higher than that in the blank electrolyte at the same potential (78 mA cm^{-2} , purple line), verifying that NO_3^- participates in the reduction reaction. The $i-t$ tests were carried out from -0.29 to -0.69 V (Fig. S5). The absorbance of the diluted electrolyte was detected by UV-visible (UV-Vis) spectrophotometry (Fig. S6). The ammonia yield and FE were further calculated from the standard curve (Figs. S7–9). With continuously decreasing application potential, the

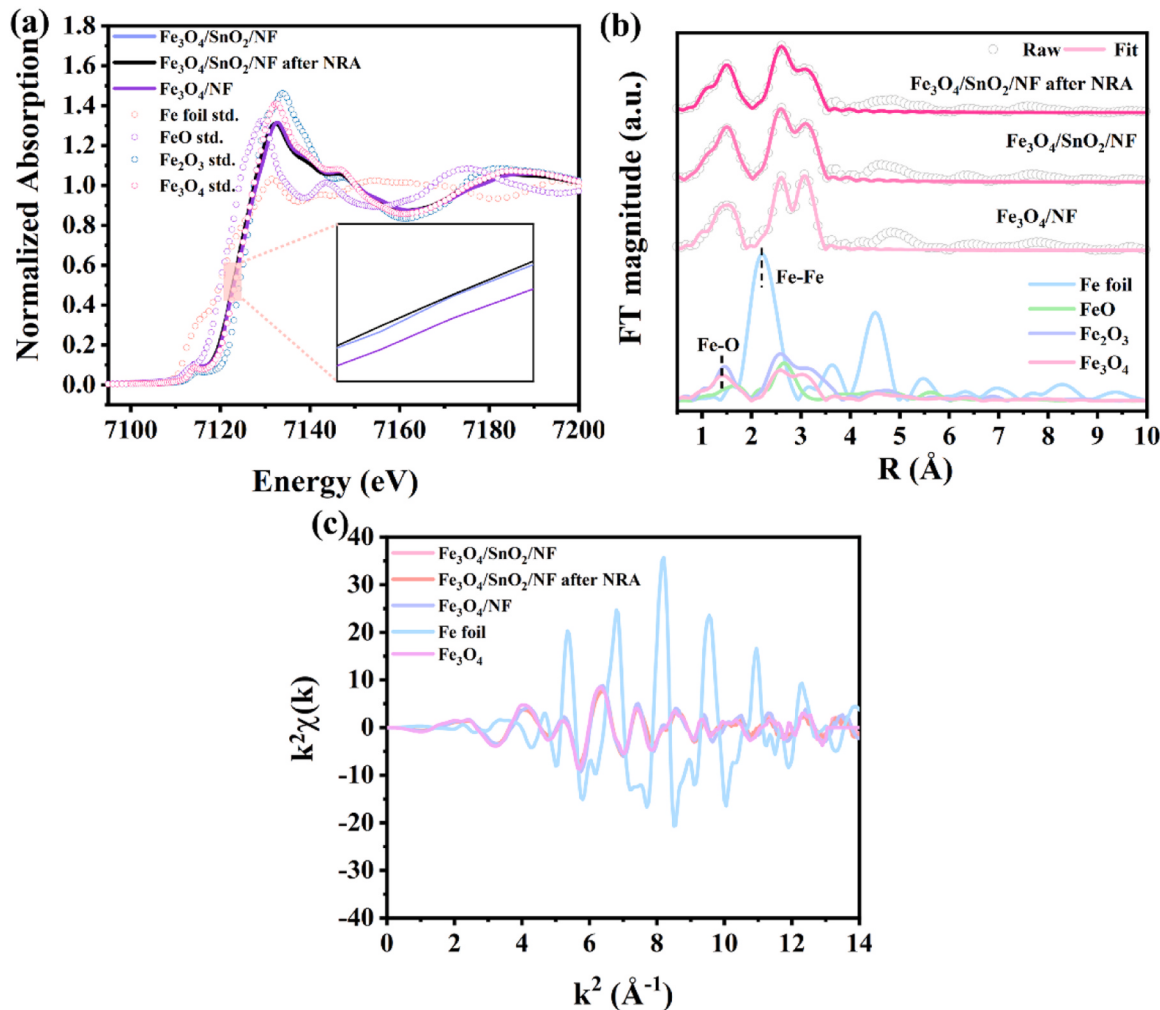


Fig. 3. (a) XANES spectra of the Fe K-edge (the inset is the enlarged absorption edge). (b) The k^3 -weighted Fourier-transformed EXAFS R-space patterns. (c) Oscillation plots of EXAFS.

ammonia yield and NO_3^- conversion are gradually increasing. However, FE shows a volcanic trend (Fig. 4b and c) due to the gradual enhancement of the competitive HER. At -0.49 V , FE, ammonia yield, ammonia selectivity, and NO_3^- conversion of $\text{Fe}_3\text{O}_4/\text{SnO}_2/\text{NF}$ reached 98.78%, $0.2548 \text{ mmol h}^{-1} \text{ cm}^{-2}$, 98.85%, and 90.19%, respectively. The NRA performance of $\text{Fe}_3\text{O}_4/\text{SnO}_2/\text{NF}$ is superior to most of the catalysts reported so far (Table S3). The NO_2^- selectivity shows a clear downhill trend at more negative potential, which only reached 0.3896% at -0.49 V , much smaller than ammonia selectivity (98.85%, Fig. 4d). Fig. 4e reveals that the NO_2^- is detected only in the lower potential range ($-0.29 \sim -0.49 \text{ V}$). Besides, during the time-dependent NRA electrolysis (Fig. S10), NO_3^- -N concentration drops dramatically while NH_3 -N concentration increases significantly. The concentration of NO_2^- shows a volcano trend, suggesting that the NO_3^- is firstly reduced to NO_2^- and then progressively hydrogenated to NH_3 during the NRA process.

The ammonia yields of $\text{Fe}_3\text{O}_4/\text{SnO}_2/\text{NF}$ were tested in the electrolyte containing 200 ppm KNO_3 -N and no KNO_3 . In addition, the ammonia yields of the pure NF and the open circuit potential (OCP) were tested. Ammonia yields are negligible in the blank electrolyte, the OCP conditions, and the pure NF (Fig. S11). This result proves that the ammonia production originates from the electrochemical NO_3^- reduction. Isotope labeling experiments were conducted to further examine the origin of ammonia production, employing $^{15}\text{NO}_3^-$ and $^{14}\text{NO}_3^-$ as the additive electrolyte. The ^1H NMR spectrum of $^{15}\text{NH}_4^+$ shows double peaks, while $^{14}\text{NH}_4^+$ shows triple peaks, which suggests that ammonia is exclusively

derived from NO_3^- reduction (Fig. 4f) [48]. In order to comprehensively evaluate the NRA performance for $\text{Fe}_3\text{O}_4/\text{SnO}_2/\text{NF}$, the contrastive catalysts including $\text{Fe}_3\text{O}_4/\text{NF}$ and SnO_2/NF were measured. Notably, the current density of $\text{Fe}_3\text{O}_4/\text{NF}$, SnO_2/NF , and $\text{Fe}_3\text{O}_4/\text{SnO}_2/\text{NF}$ is obviously different (Fig. 5a). Compared to other contrastive catalysts, $\text{Fe}_3\text{O}_4/\text{SnO}_2/\text{NF}$ exhibits more positive onset potential and higher current density, suggesting that $\text{Fe}_3\text{O}_4/\text{SnO}_2/\text{NF}$ has more excellent electrocatalytic activity for nitrate reduction. As shown in Fig. 5b and c, the FE (98.78%), NH_3 yield ($0.2548 \text{ mmol h}^{-1} \text{ cm}^{-2}$), and NO_3^- conversion (90.19%) of $\text{Fe}_3\text{O}_4/\text{SnO}_2/\text{NF}$ at -0.49 V are much higher than those of $\text{Fe}_3\text{O}_4/\text{NF}$ (77.61%, $0.0806 \text{ mmol h}^{-1} \text{ cm}^{-2}$ and 40.64%, Fig. S12) and SnO_2/NF (45.60%, $0.0142 \text{ mmol h}^{-1} \text{ cm}^{-2}$ and 14.10%, Fig. S13). Moreover, the NO_2^- selectivity of $\text{Fe}_3\text{O}_4/\text{NF}$ and SnO_2/NF respectively reaches 11.50% and 13.05% at -0.49 V , which is more than 30 times greater than that of $\text{Fe}_3\text{O}_4/\text{SnO}_2/\text{NF}$ (Fig. 5d). These results indicate that the formation of the heterointerfaces inhibits the generation of byproducts (NO_2^-) and favors the production of NH_3 . Namely, the construction of heterointerfaces is a promising strategy to improve the NRA performance.

In order to reveal the origin of the excellent catalytic performance of $\text{Fe}_3\text{O}_4/\text{SnO}_2/\text{NF}$, the ECSA of the catalyst was evaluated by C_{dl} tests (Figs. S14–16). The C_{dl} of $\text{Fe}_3\text{O}_4/\text{SnO}_2/\text{NF}$ is significantly higher than that of $\text{Fe}_3\text{O}_4/\text{NF}$ and SnO_2/NF , indicating that $\text{Fe}_3\text{O}_4/\text{SnO}_2/\text{NF}$ owns larger active area and could expose more redox active sites. In addition, the EIS tests show that the charge transfer resistance of $\text{Fe}_3\text{O}_4/\text{SnO}_2/\text{NF}$

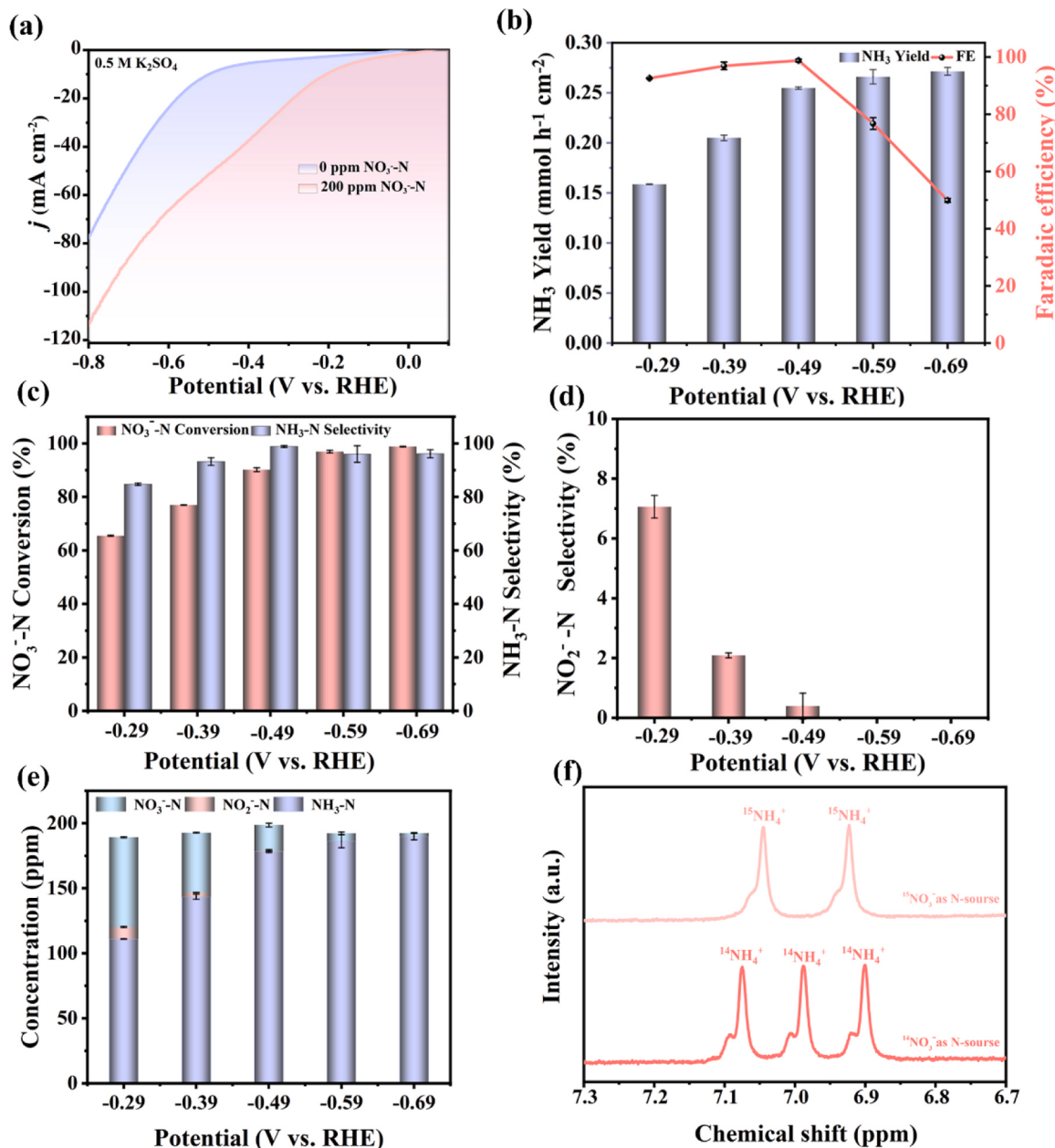


Fig. 4. (a) LSV curves of $\text{Fe}_3\text{O}_4/\text{SnO}_2/\text{NF}$ tested in $0.5 \text{ M } \text{K}_2\text{SO}_4 + 200 \text{ ppm } \text{KNO}_3$ and blank electrolyte. (b) NH_3 yield and NH_3 -FE, (c) NO_3^- conversion and NH_3 -N selectivity, (d) NO_2^- selectivity of $\text{Fe}_3\text{O}_4/\text{SnO}_2/\text{NF}$, (e) Concentration of different products after NRA electrolysis at various potentials. (f) ^1H NMR measurements fed by $^{14}\text{NO}_3^-/^{15}\text{NO}_3^-$ after NRA.

is lower than that of $\text{Fe}_3\text{O}_4/\text{NF}$ and SnO_2/NF , demonstrating that $\text{Fe}_3\text{O}_4/\text{SnO}_2/\text{NF}$ possesses better electron transport capability and thus favors the production of ammonia from a kinetic point of view (Fig. S17). To demonstrate that the Fe sites in $\text{Fe}_3\text{O}_4/\text{SnO}_2/\text{NF}$ are active sites of NRA, the poisoning experiment was carried out using a stronger Lewis base, potassium thiocyanide (KSCN) [49,50]. As shown in Figs. 6a and 6b, after adding SCN^- ions into the K_2SO_4 solution containing NO_3^- , the current density of NRA decreases significantly due to the poisoning of the Fe sites by SCN^- . Correspondingly, the NH_3 yield also drops dramatically, while the current density of HER remains almost unchanged. This is due to the fact that the Fermi energy levels of Fe_3O_4 and SnO_2 are significantly different, the self-driven electron donation from Fe_3O_4 to SnO_2 can induce local charge redistribution around the $\text{Fe}_3\text{O}_4/\text{SnO}_2$ heterointerfaces and endows the surface of Fe_3O_4 with an electrophilic region, while the surface of SnO_2 is nucleophilic [45]. As a result, the positively charged Fe_3O_4 surface is more favorable for

adsorption of electron-rich NO_3^- , while the negatively charged SnO_2 surface is more favorable for adsorption of $^*\text{H}$. Thus, the Fe sites are poisoned due to preferentially occupied by the stronger Lewis base SCN^- in the presence of SCN^- , whereas the Sn sites are hardly poisoned and adsorbs $^*\text{H}$, which leads to a sharp decrease in the current density of NRA and the NH_3 yield, while the current density of HER remains almost unchanged. Obviously, the synergy of Fe sites and Sn sites boosts the efficiency of NRA.

To evaluate the NRA catalytic stability of $\text{Fe}_3\text{O}_4/\text{SnO}_2/\text{NF}$, the successive cycling test was performed at -0.49 V . No significant decrease in ammonia yield, FE, selectivity and NO_3^- conversion are observed after 11 cycles (Figs. 6c, 6d and S18). Meanwhile, the nanosheet structure of $\text{Fe}_3\text{O}_4/\text{SnO}_2/\text{NF}$ shows no apparent changes after the cyclic stability tests, and the phase remains unchanged (Fig. S19). The above results suggest that $\text{Fe}_3\text{O}_4/\text{SnO}_2/\text{NF}$ has admirable catalytic stability and structural stability for NRA. As shown in Figs. S20a and 20b, the NRA

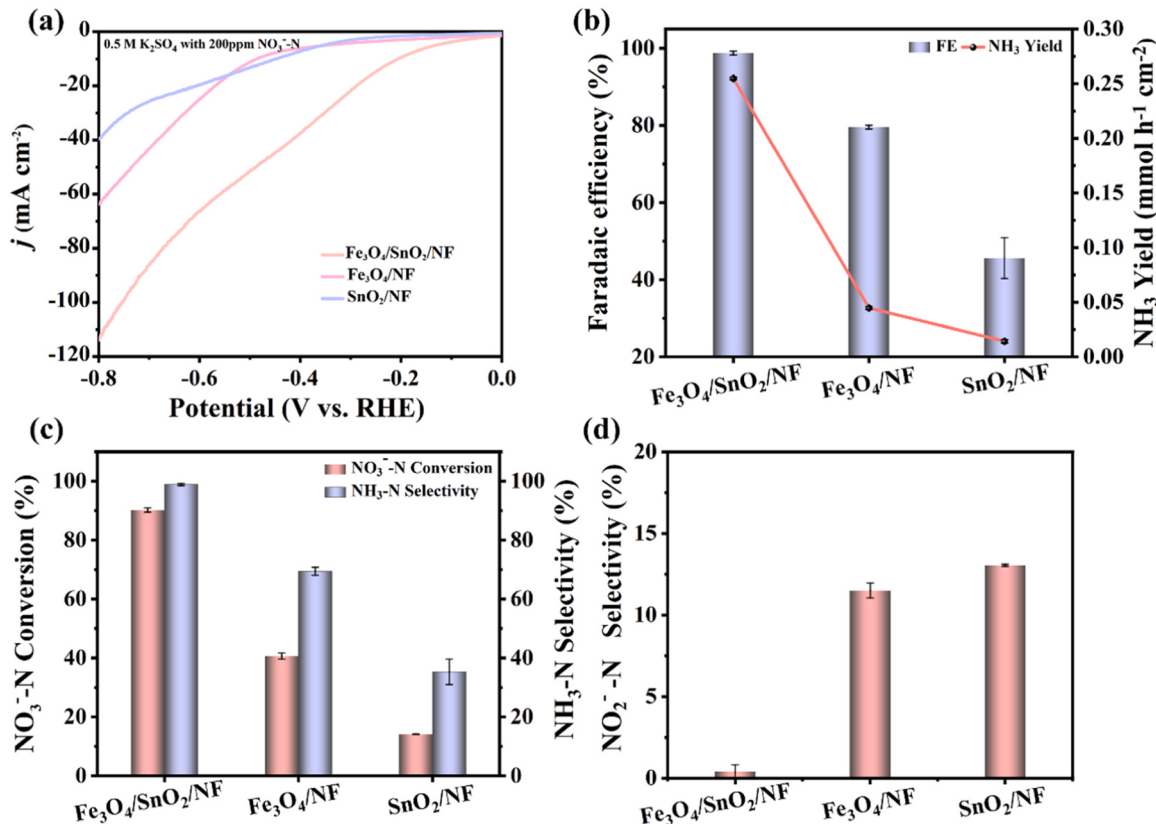


Fig. 5. (a) LSV curves, (b) Faradaic efficiency and NH_3 yield rates, (c) NO_3^- -N conversion and NH_3 -N selectivity, (d) NO_2^- -N selectivity of three samples.

tests were conducted for 1 and 2 h at nitrate concentrations of 500 ppm, 1000 ppm, and 1400 ppm, respectively. The results showed that the NRA performance of $\text{Fe}_3\text{O}_4/\text{SnO}_2/\text{NF}$ was not satisfactory and was not as good as that at nitrate concentrations of 200 ppm. To investigate the effect of impurities on catalyst performance, the NRA performance testing of the as-prepared catalyst in the presence of other coexisting ions were performed (Figs. S20c and 20d). In the presence of impurities (including CO_3^{2-} , Na^+ , Cl^- , ClO_4^- , HCO_3^- , Li^+ , and their concentration is 200 ppm), the NRA performance and selectivity of the catalyst remain excellent, indicating its potential for application.

3.3. Mechanism investigation

To further reveal the high activity origin of the $\text{Fe}_3\text{O}_4/\text{SnO}_2/\text{NF}$ catalyst, the DFT calculations were performed. Based on the TEM characterization results (Fig. 1 f), the (220) of Fe_3O_4 and (110) of SnO_2 planes were selected as the calculated models (Figs. S21 and S22). The project density of states (PDOS) in Fig. 7a shows that the level of the d-band center of $\text{Fe}_3\text{O}_4/\text{SnO}_2/\text{NF}$ is closer to the Fermi energy level compared to $\text{Fe}_3\text{O}_4/\text{NF}$, indicating that the formation of heterointerfaces in $\text{Fe}_3\text{O}_4/\text{SnO}_2/\text{NF}$ enhances the absorption of nitrate and NRA intermediates. Due to the need for protons in NRA, the moderate HER activity of the catalyst is beneficial to NRA (water in the electrolyte serves as the proton source). Therefore, the adsorption energy, dissociation energy, and H_2 generation energy of water molecules at the Fe and Sn sites were calculated separately, and the results are shown in Figs. 7b and S23. Apparently, these energies at the Fe sites are much higher than those at the Sn sites [3,18], indicating that the Sn sites are more favorable to HER, and thus Sn rather than Fe is the active site of HER. From an energy perspective, the Fe sites with NRA activity are not conducive to HER. These findings reveal that Fe on $\text{Fe}_3\text{O}_4/\text{SnO}_2/\text{NF}$ is the primary active site facilitating the adsorption and activation of NO_3^- and inhibiting the HER side reaction, while Sn is the active site of HER to

provide ${}^*\text{H}$. In a word, this synergistic effect of Fe and Sn sites contributes to the excellent NRA activity and selectivity of $\text{Fe}_3\text{O}_4/\text{SnO}_2/\text{NF}$ with heterointerfaces.

The intermediates of the reaction process were monitored by in situ Raman. As shown in Fig. S24, the peak strength of 982 cm^{-1} corresponds to SO_4^{2-} from the electrolyte. Several peaks at 1011 , 1186 , and 1450 cm^{-1} are observed, which can be assigned to the NO_3^- stretching vibration of absorbed NO_3^- , the stretching vibration of NO_2^- , and the stretching vibration of $\text{N} = \text{O}$, respectively.[51] The two signals located at 1140 and 1516 cm^{-1} respectively come from the NH_2 wagging and NH bending, whose intensities increase over potential.[52] The peak near 1584 cm^{-1} is the HNH bending vibration of NH_3 and its intensity is weak, indicating that the generated NH_3 can quickly desorb from the catalyst surface, which is beneficial for NRA.[53,54] Based on the above findings, a potential NRA mechanism is proposed. First, NO_3^- is adsorbed on the catalyst surface and reduced to the intermediate product ${}^*\text{NO}_2$ (* denotes the state of being adsorbed) [22,28]. Then, ${}^*\text{NO}_2$ undergoes a deoxidation reaction to form ${}^*\text{NO}$. Through gradual hydrogenation, ${}^*\text{NO}$ may form ${}^*\text{NOH}$ (Pathway 1) and ${}^*\text{NHO}$ (Pathway 2). The ${}^*\text{NOH}$ and ${}^*\text{NHO}$ intermediates undergo a stepwise hydrogenation reaction (Pathway 1: ${}^*\text{NOH} \rightarrow {}^*\text{N} \rightarrow {}^*\text{NH} \rightarrow {}^*\text{NH}_2 \rightarrow {}^*\text{NH}_3 \rightarrow \text{NH}_3$, Pathway 2: ${}^*\text{NHO} \rightarrow {}^*\text{NHOH} \rightarrow {}^*\text{NH} \rightarrow {}^*\text{NH}_2 \rightarrow {}^*\text{NH}_3 \rightarrow \text{NH}_3$) to generate NH_3 . Thus, ${}^*\text{H}$ produced by H_2O dissociation embodies a critical role in NRA. The Gibbs free energy changes (ΔG) of NRA pathways on $\text{Fe}_3\text{O}_4/\text{SnO}_2$ were calculated. The intermediates associated with Pathway 1 and Pathway 2 of NRA were calculated on $\text{Fe}_3\text{O}_4/\text{SnO}_2$, and the related structures of the NRA intermediates are shown in Fig. 7c (inset). In Pathway 1, a high ΔG of 1.32 eV is obtained for the rate-determining step (RDS) from ${}^*\text{NO}$ to ${}^*\text{NOH}$. From a thermodynamic perspective, Pathway 2 is more favorable on $\text{Fe}_3\text{O}_4/\text{SnO}_2$. As depicted in Figs. S25 and S26, for the steps ${}^*\text{N} + \text{NO}_3^- \rightarrow {}^*\text{NO}_3$ on Fe_3O_4 and ${}^*\text{NH}_3 \rightarrow \text{NH}_3$ on SnO_2 , the calculated ΔG are respectively 1.58 and 3.43 eV , while that of these two steps on $\text{Fe}_3\text{O}_4/\text{SnO}_2$ are only 0.66 and 0.86 eV . These results

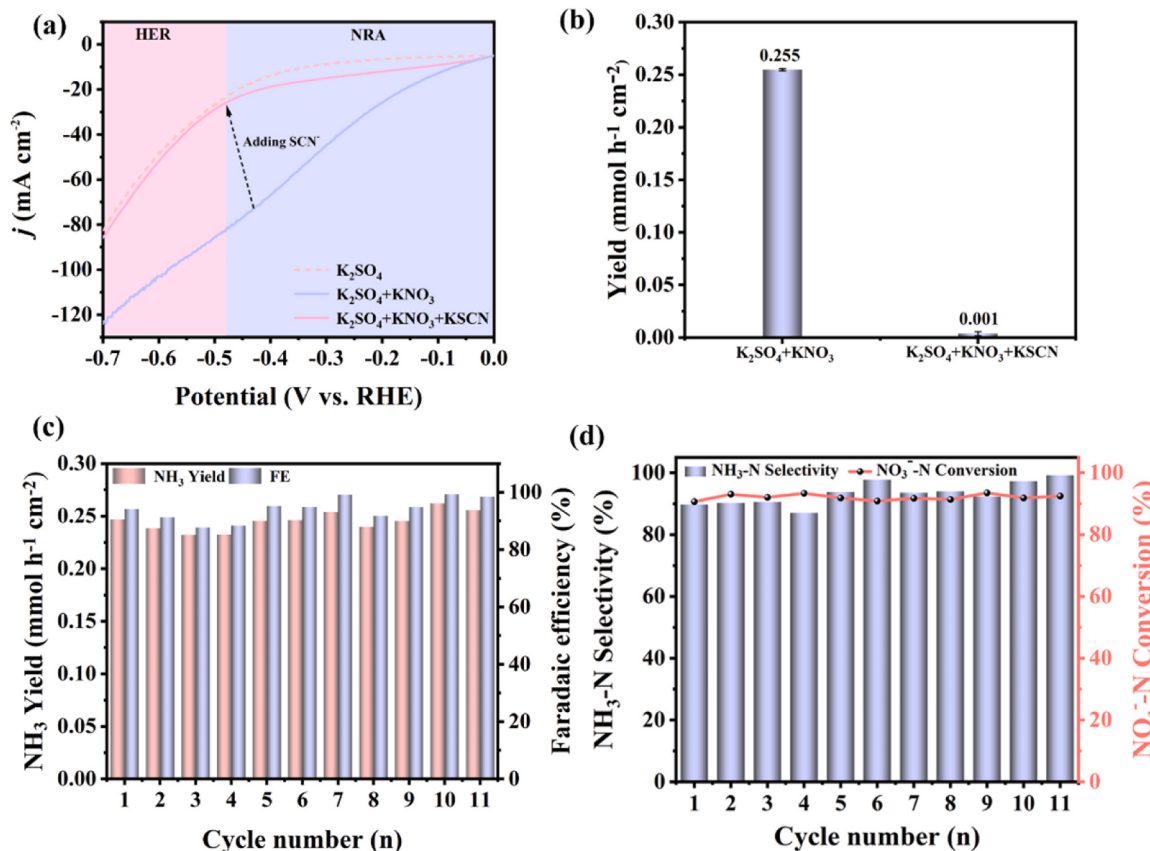


Fig. 6. (a) LSV curves for poisoning experiment on $\text{Fe}_3\text{O}_4/\text{SnO}_2/\text{NF}$. (b) NH_3 Yield with SCN^- and without SCN^- . (c) Faradaic efficiency and NH_3 yield, (d) NH_3 -N selectivity and NO_3^- -N conversion for 11 consecutive cycles.

indicate that $\text{Fe}_3\text{O}_4/\text{SnO}_2$ possesses moderate $^*\text{NO}_3$ adsorption strength and $^*\text{NH}_3$ desorption strength. Therefore, $\text{Fe}_3\text{O}_4/\text{SnO}_2/\text{NF}$ catalysts with heterointerfaces are more beneficial for NRA.

In addition, the electrostatic potential of SnO_2 (110) and Fe_3O_4 (220) in the z direction was calculated. The static potential can be used not only as a work function ($\Phi = E_{\text{vac}} - E_F$), but also as a powerful tool to analyze the surface electronic structure, such as the electron flow in the heterojunction model [55]. As shown in Fig. S27, the work functions of SnO_2 (110) surface ($\Phi_{\text{SnO}_2} = 7.07$ eV) and Fe_3O_4 (220) surface ($\Phi_{\text{Fe}_3\text{O}_4} = 5.55$ eV) are compared, and the Fermi energy of SnO_2 is found to be lower than that of Fe_3O_4 surface. Thus, in the $\text{Fe}_3\text{O}_4/\text{SnO}_2$ heterointerfaces, electron will transfer from Fe_3O_4 to SnO_2 until the two Fermi energies reach the same level (-1.77 eV) [45,56,57], which is consistent with the XPS results.

On the basis of all the above results, a synergistic catalysis mechanism of $\text{Fe}_3\text{O}_4/\text{SnO}_2/\text{NF}$ for NRA is concluded. The Sn sites encourage the dissociation of water and enhance the coverage of $^*\text{H}$ on $\text{Fe}_3\text{O}_4/\text{SnO}_2/\text{NF}$, while the Fe sites adsorb and activate nitrate throughout the NRA electrochemical reaction. The produced $^*\text{H}$ from Sn sites is provided to Fe sites, thus accelerates the hydrogenation reaction of intermediates and enhances the NRA activity of $\text{Fe}_3\text{O}_4/\text{SnO}_2/\text{NF}$. In addition, $\text{Fe}_3\text{O}_4/\text{SnO}_2/\text{NF}$ optimizes the adsorption of reaction intermediates, prevents the generation of byproducts NO_2^- and inhibits the occurrence of HER.

4. Conclusions

In conclusion, $\text{Fe}_3\text{O}_4/\text{SnO}_2/\text{NF}$ with heterointerfaces was designed and constructed for NRA. The electronic interaction at heterointerfaces induces charge redistribution, thus improving the performance of NRA. $\text{Fe}_3\text{O}_4/\text{SnO}_2/\text{NF}$ showed excellent performance at -0.49 V. (NH_3

Faradaic efficiency: 98.78%, NH_3 yield: 0.2584 mmol h $^{-1}$ cm $^{-2}$, NH_3 selectivity: 98.85%, and NO_3^- conversion: 90.19%), which is significantly better than $\text{Fe}_3\text{O}_4/\text{NF}$ and SnO_2/NF . Combining experimental and theoretical calculations, the synergistic catalytic mechanism of $\text{Fe}_3\text{O}_4/\text{SnO}_2/\text{NF}$ was revealed, in which the Fe sites activate nitrate while the Sn sites accelerate H_2O dissociation and provide sufficient $^*\text{H}$ to facilitate further hydrogenation process. This work reveals the essence of heterointerface engineering to activate nitrate, optimize the adsorption of NRA intermediates, and inhibit the occurrence of side reactions, which has guiding significance for the design and preparation of highly efficient NRA catalysts.

CRediT authorship contribution statement

Gou Qiao: Writing – original draft, Validation, Methodology, Investigation, Data curation. **He Rongxing:** Writing – review & editing, Resources, Funding acquisition, Formal analysis. **Wang Yun:** Software, Resources, Investigation. **Li Ming:** Methodology, Conceptualization. **Shen Wei:** Software, Resources, Investigation. **Jiang Yimin:** Resources, Investigation. **Gou Fenglin:** Software, Resources, Investigation. **Lv Shengmei:** Software, Resources, Investigation. **Mao Yini:** Software, Resources, Investigation.

Declaration of Competing Interest

The authors declare that they have no known competing financial interests or personal relationships that could have appeared to influence the work reported in this paper.

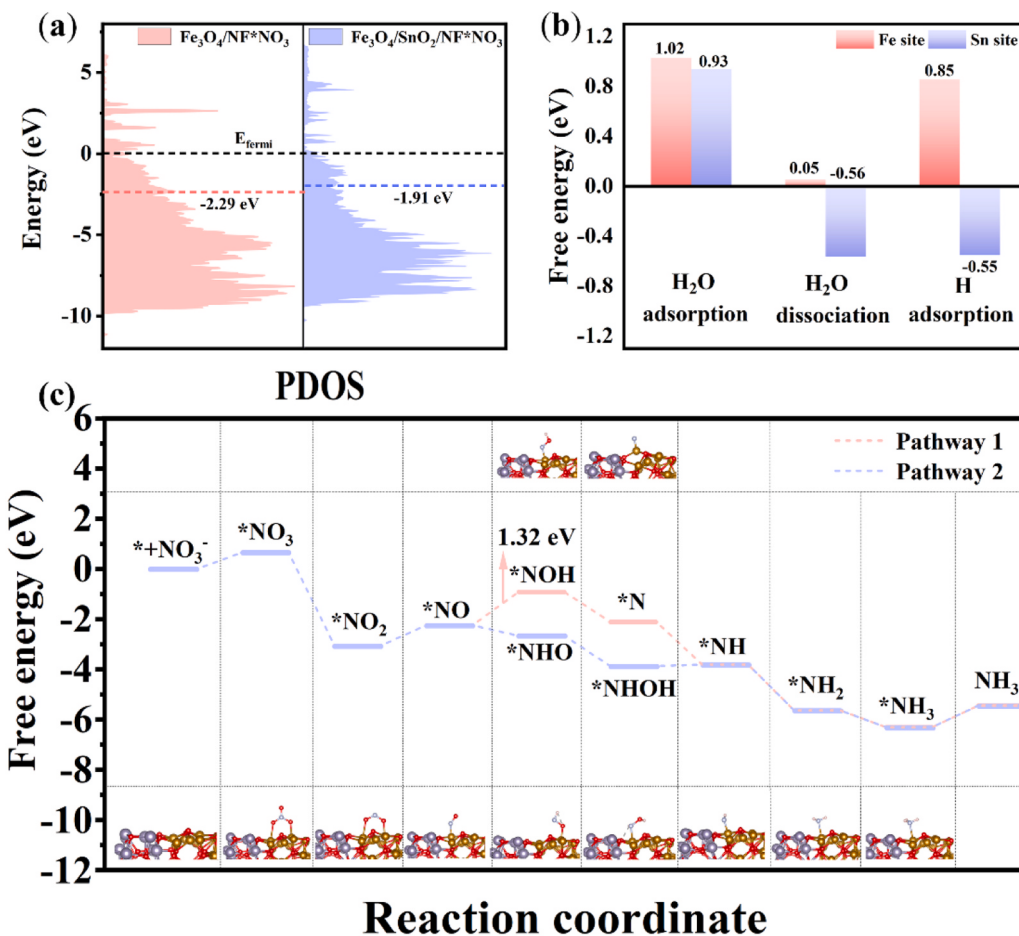


Fig. 7. (a) Project density of states of Fe_3O_4 and $\text{Fe}_3\text{O}_4/\text{SnO}_2$ after adsorption of $^*\text{NO}_3$. (The dashed lines are the position of the d-band center). (b) HER pathways on Fe and Sn sites of $\text{Fe}_3\text{O}_4/\text{SnO}_2$. (c) Free energy changes of the NRA reaction for different intermediates of two pathways on $\text{Fe}_3\text{O}_4/\text{SnO}_2$.

Data availability

Data will be made available on request.

Acknowledgements

We acknowledge the financial supports from the National Natural Science Foundation of China (22006120), the Innovation Research 2035 Pilot Plan of Southwest University (SWU-XDZD22011) and the Program for Innovation Team Building at Institutions of Higher Education in Chongqing (CXTDX201601011). The authors would like to thank Hongyu Cheng (from Shitianjia Lab (www.shitianjia.com) for the XPS and TEM analysis.

Appendix A. Supporting information

Supplementary data associated with this article can be found in the online version at [doi:10.1016/j.apcatb.2024.123810](https://doi.org/10.1016/j.apcatb.2024.123810).

References

- [1] J. Lim, C.A. Fernández, S.W. Lee, M.C. Hatzell, Ammonia and nitric acid demands for fertilizer use in 2050, *ACS Energy Lett.* 6 (10) (2021) 3676–3685, <https://doi.org/10.1021/acsenergylett.1c01614>.
- [2] J. Feng, H. Pan, Electronic state optimization for electrochemical N_2 reduction reaction in aqueous solution, *J. Mater. Chem. A* 8 (28) (2020) 13896–13915, <https://doi.org/10.1039/d0ta04709k>.
- [3] G. Zhang, X. Li, K. Chen, Y. Guo, D. Ma, K. Chu, Tandem electrocatalytic nitrate reduction to ammonia on MBenes, *Angew. Chem. Int. Ed.* 62 (13) (2023) e202300054, <https://doi.org/10.1002/anie.202300054>.
- [4] Y. Li, H. Wang, C. Priest, S. Li, P. Xu, G. Wu, Advanced electrocatalysis for energy and environmental sustainability via water and nitrogen reactions, *Adv. Mater.* 33 (6) (2021) e2000381, <https://doi.org/10.1002/adma.202000381>.
- [5] X. Zhao, G. Hu, G.F. Chen, H. Zhang, S. Zhang, H. Wang, Comprehensive understanding of the thriving ambient electrochemical nitrogen reduction reaction, *Adv. Mater.* 33 (33) (2021) e2007650, <https://doi.org/10.1002/adma.202007650>.
- [6] Y. Ren, C. Yu, X. Tan, H. Huang, Q. Wei, J. Qiu, Strategies to suppress hydrogen evolution for highly selective electrocatalytic nitrogen reduction: challenges and perspectives, *Energy Environ. Sci.* 14 (3) (2021) 1176–1193, <https://doi.org/10.1039/d0ee03596c>.
- [7] L. Ouyang, J. Liang, Y. Luo, D. Zheng, S. Sun, Q. Liu, M.S. Hamdy, X. Sun, B. Ying, Recent advances in electrocatalytic ammonia synthesis, *Chin. J. Catal.* 50 (2023) 6–44, [https://doi.org/10.1016/S1872-2067\(23\)64464-X](https://doi.org/10.1016/S1872-2067(23)64464-X).
- [8] J. Liang, Z. Li, L. Zhang, X. He, Y. Luo, D. Zheng, Y. Wang, T. Li, H. Yan, B. Ying, S. Sun, Q. Liu, M.S. Hamdy, B. Tang, X. Sun, Advances in ammonia electrosynthesis from ambient nitrate/nitrite reduction, *Chem* 9 (7) (2023) 1768–1827, <https://doi.org/10.1016/j.chempr.2023.05.037>.
- [9] P.H. van Langevelde, I. Katsounaros, M.T.M. Koper, Electrocatalytic nitrate reduction for sustainable ammonia production, *Joule* 5 (2) (2021) 290–294, <https://doi.org/10.1016/j.joule.2020.12.025>.
- [10] J. Li, G. Zhan, J. Yang, F. Quan, C. Mao, Y. Liu, B. Wang, F. Lei, L. Li, A.W.M. Chan, L. Xu, Y. Shi, Y. Du, W. Hao, P.K. Wong, J. Wang, S.X. Dou, L. Zhang, J.C. Yu, Efficient ammonia electrosynthesis from nitrate on strained ruthenium nanoclusters, *J. Am. Chem. Soc.* 142 (15) (2020) 7036–7046, <https://doi.org/10.1021/jacs.0c00418>.
- [11] D. Liu, M. Chen, X. Du, H. Ai, K.H. Lo, S. Wang, S. Chen, G. Xing, X. Wang, H. Pan, Development of electrocatalysts for efficient nitrogen reduction reaction under ambient condition, *Adv. Funct. Mater.* 31 (11) (2020), <https://doi.org/10.1002/adfm.202000893>.
- [12] X. Fan, C. Liu, Z. Li, Z. Cai, L. Ouyang, Z. Li, X. He, Y. Luo, D. Zheng, S. Sun, Y. Wang, B. Ying, Q. Liu, A. Farouk, M.S. Hamdy, F. Gong, X. Sun, Y. Zheng, Pd-doped Co_3O_4 nanoarray for efficient eight-electron nitrate electrocatalytic reduction to ammonia synthesis, *Small* 19 (42) (2023) 2303424, <https://doi.org/10.1002/smll.202303424>.
- [13] D. Liu, L. Qiao, S. Peng, H. Bai, C. Liu, W.F. Ip, K.H. Lo, H. Liu, K.W. Ng, S. Wang, X. Yang, H. Pan, Recent advances in electrocatalysts for efficient nitrate reduction

to ammonia, *Adv. Funct. Mater.* 59 (13) (2023) 5350–5354, <https://doi.org/10.1002/adfm.202303480>.

[14] Y. Wang, W. Zhou, R. Jia, Y. Yu, B. Zhang, Unveiling the activity origin of a copper-based electrocatalyst for selective nitrate reduction to ammonia, *Angew. Chem. Int. Ed.* 59 (13) (2020) 5350–5354, <https://doi.org/10.1002/anie.201915992>.

[15] Q. Gao, H.S. Pillai, Y. Huang, S. Liu, Q. Mu, X. Han, Z. Yan, H. Zhou, Q. He, H. Xin, H. Zhu, Breaking adsorption-energy scaling limitations of electrocatalytic nitrate reduction on intermetallic CuPd nanocubes by machine-learned insights, *Nat. Commun.* 13 (1) (2022) 2338, <https://doi.org/10.1038/s41467-022-29926-w>.

[16] Z.Y. Wu, M. Karamad, X. Yong, Q. Huang, D.A. Cullen, P. Zhu, C. Xia, Q. Xiao, M. Shakouri, F.Y. Chen, J.Y.T. Kim, Y. Xia, K. Heck, Y. Hu, M.S. Wong, Q. Li, I. Gates, S. Siahrostami, H. Wang, Electrochemical ammonia synthesis via nitrate reduction on Fe single atom catalyst, *Nat. Commun.* 12 (1) (2021) 2870, <https://doi.org/10.1038/s41467-021-23115-x>.

[17] J. Zhou, M. Wen, R. Huang, Q. Wu, Y. Luo, Y. Tian, G. Wei, Y. Fu, Regulating active hydrogen adsorbed on grain boundary defects of nano-nickel for boosting ammonia electrosynthesis from nitrate, *Energy Environ. Sci.* 16 (6) (2023) 2611–2620, <https://doi.org/10.1039/d2ee04095f>.

[18] J. Li, G. Zhan, J. Yang, F. Quan, C. Mao, Y. Liu, B. Wang, F. Lei, L. Li, A.W.M. Chan, L. Xu, Y. Shi, Y. Du, W. Hao, P.K. Wong, J. Wang, S.-X. Dou, L. Zhang, J.C. Yu, Efficient ammonia electrosynthesis from nitrate on strained ruthenium nanoclusters, *J. Am. Chem. Soc.* 142 (15) (2020) 7036–7046, <https://doi.org/10.1021/jacs.0c00418>.

[19] G. Zhang, X. Li, K. Chen, Y. Guo, D. Ma, K. Chu, Tandem electrocatalytic nitrate reduction to ammonia on MBenes, *Angew. Chem. Int. Ed.* 62 (13) (2023), <https://doi.org/10.1002/anie.202300054>.

[20] Q. Gao, H.S. Pillai, Y. Huang, S. Liu, Q. Mu, X. Han, Z. Yan, H. Zhou, Q. He, H. Xin, H. Zhu, Breaking adsorption-energy scaling limitations of electrocatalytic nitrate reduction on intermetallic CuPd nanocubes by machine-learned insights, *Nat. Commun.* 13 (1) (2022) 2338, <https://doi.org/10.1038/s41467-022-29926-w>.

[21] X. Liu, C. Liu, X. He, Z. Cai, K. Dong, J. Li, X. Fan, T. Xie, X. Yang, Y. Luo, D. Zheng, S. Sun, S. Alfaifi, F. Gong, X. Sun, Fe-doped Co₃O₄ nanowire struttet 3D pinewood-derived carbon: a highly selective electrocatalyst for ammonia production via nitrate reduction, *Nano Res.* (2023), <https://doi.org/10.1007/s12274-023-6204-y>.

[22] C. Wang, Y. Zhang, H. Luo, H. Zhang, W. Li, W.X. Zhang, J. Yang, Iron-based nanocatalysts for electrochemical nitrate reduction, *Small Methods* 6 (10) (2022) e2200790, <https://doi.org/10.1002/smtd.202200790>.

[23] S. Meng, S. Sun, Y. Liu, Y. Lu, M. Chen, Synergistic modulation of inverse spinel Fe₃O₄ by doping with chromium and nitrogen for efficient electrocatalytic water splitting, *J. Colloid Interface Sci.* 624 (2022) 433–442, <https://doi.org/10.1016/j.jcis.2022.04.141>.

[24] W. Xu, W. Zhong, C. Yang, R. Zhao, J. Wu, X. Li, N. Yang, Tailoring interfacial electron redistribution of Ni/Fe₃O₄ electrocatalysts for superior overall water splitting, *J. Energy Chem.* 73 (2022) 330–338, <https://doi.org/10.1016/j.jec.2022.06.042>.

[25] J.A.S.B. Cardoso, B. Šljukić, E. Kayhan, C.A.C. Sequeira, D.M.F. Santos, Palladium-nickel on tin oxide-carbon composite supports for electrocatalytic hydrogen evolution, *Catal. Today* 357 (2020) 302–310, <https://doi.org/10.1016/j.cattod.2019.05.056>.

[26] L.-H. Xing, X.-T. Shi, Y.-X. Wang, L. Zhang, X.-Y. Xu, F.-X. Meng, J. Li, Electrochemical synthesis of Ni-SnO₂ composite electrodes for hydrogen evolution reaction in alkaline solution, *Int. J. Electrochem. Sci.* 17 (5) (2022) 220530, <https://doi.org/10.20964/2022.05.35>.

[27] S. Pan, X. Yang, J. Sun, X. Wang, J. Zhu, Y. Fu, Competitive adsorption mechanism of defect-induced d-orbital single electrons in SrRuO₃ for alkaline hydrogen evolution reaction, *Adv. Energy Mater.* 13 (38) (2023) 2301779, <https://doi.org/10.1002/aenm.202301779>.

[28] S. Liu, L. Cui, S. Yin, H. Ren, Z. Wang, Y. Xu, X. Li, L. Wang, H. Wang, Heterointerface-triggered electronic structure reformation: Pd/CuO nano-olives motivate nitrite electroreduction to ammonia, *Appl. Catal. B Environ.* 319 (2022), <https://doi.org/10.1016/j.apcatb.2022.121876>.

[29] W. Zhu, F. Yao, Q. Wu, Q. Jiang, J. Wang, Z. Wang, H. Liang, Weakened d-p orbital hybridization in *in situ* reconstructed Ru/β-Co(OH)₂ heterointerfaces for accelerated ammonia electrosynthesis from nitrates, *Energy Environ. Sci.* 16 (6) (2023) 2483–2493, <https://doi.org/10.1039/d3ee00371j>.

[30] Z. Shu, H. Chen, X. Liu, H. Jia, H. Yan, Y. Cai, High-throughput screening of heterogeneous transition metal dual-atom catalysts by synergistic effect for nitrate reduction to ammonia, *Adv. Funct. Mater.* 33 (32) (2023), <https://doi.org/10.1002/adfm.202301493>.

[31] C. Feng, W. Zhou, H. Wu, Q. Huo, J. Shao, X. Li, H. Yang, Q. Hu, C. He, Tuning work function difference of copper/cobalt oxides heterointerfaces enables efficient electrochemical nitrate reduction, *Appl. Catal. B Environ.* 341 (2024), <https://doi.org/10.1016/j.apcatb.2023.123280>.

[32] Y. Mao, Y. Jiang, H. Liu, Y. Jiang, M. Li, W. Su, R. He, Ambient electrocatalytic synthesis of urea by co-reduction of NO₃⁻ and CO₂ over graphene-supported In₂O₃, *Chin. Chem. Lett.* 35 (3) (2024) 108540, <https://doi.org/10.1016/j.cclet.2023.108540>.

[33] G. Kresse, J. Hafner, Ab initiomolecular-dynamics simulation of the liquid-metal-amorphous-semiconductor transition in germanium, *Phys. Rev. B* 49 (20) (1994) 14251–14269, <https://doi.org/10.1103/PhysRevB.49.14251>.

[34] P.E. Blöchl, Projector augmented-wave method, *Phys. Rev. B* 50 (24) (1994) 17953–17979, <https://doi.org/10.1103/PhysRevB.50.17953>.

[35] J.P. Perdew, K. Burke, M. Ernzerhof, Generalized gradient approximation made simple, *Phys. Rev. Lett.* 77 (18) (1996) 3865–3868, <https://doi.org/10.1103/PhysRevLett.77.3865>.

[36] S.L. Dudarev, G.A. Botton, S.Y. Savrasov, C.J. Humphreys, A.P. Sutton, Electron-energy-loss spectra and the structural stability of nickel oxide: an LSDA+U study, *Phys. Rev. B* 57 (3) (1998) 1505–1509, <https://doi.org/10.1103/PhysRevB.57.1505>.

[37] H.J. Monkhorst, J.D. Pack, Special points for Brillouin-zone integrations, *Phys. Rev. B* 13 (12) (1976) 5188–5192, <https://doi.org/10.1103/PhysRevB.13.5188>.

[38] S. Guo, K. Heck, S. Kasiraju, H. Qian, Z. Zhao, L.C. Grabow, J.T. Miller, M.S. Wong, Insights into nitrate reduction over indium-decorated palladium nanoparticle catalysts, *ACS Catal.* 8 (1) (2017) 503–515, <https://doi.org/10.1021/acscatal.7b01371>.

[39] J.-X. Liu, D. Richards, N. Singh, B.R. Goldsmith, Activity and selectivity trends in electrocatalytic nitrate reduction on transition metals, *ACS Catal.* 9 (8) (2019) 7052–7064, <https://doi.org/10.1021/acscatal.9b02179>.

[40] M. Fu, Y. Mao, H. Wang, W. Luo, Y. Jiang, W. Shen, M. Li, R. He, Enhancing the electrocatalytic performance of nitrate reduction to ammonia by *in-situ* nitrogen leaching, *Chin. Chem. Lett.* 35 (2) (2024) 108341, <https://doi.org/10.1016/j.cclet.2023.108341>.

[41] X. Fan, L. Xie, J. Liang, Y. Ren, L. Zhang, L. Yue, T. Li, Y. Luo, N. Li, B. Tang, Y. Liu, S. Gao, A.A. Alshehri, Q. Liu, Q. Kong, X. Sun, *In situ* grown Fe₂O₄ particle on stainless steel: a highly efficient electrocatalyst for nitrate reduction to ammonia, *Nano Res.* 15 (4) (2021) 3050–3055, <https://doi.org/10.1007/s12274-021-3951-5>.

[42] Y. Li, Y. Liu, X. Liu, Y. Liu, Y. Cheng, P. Zhang, P. Deng, J. Deng, Z. Kang, H. Li, Fe-doped SnO₂ nanosheet for ambient electrocatalytic nitrogen reduction reaction, *Nano Res.* 15 (7) (2022) 6026–6035, <https://doi.org/10.1007/s12274-022-4298-2>.

[43] V. Mani, S. Anantharaj, S. Mishra, N. Kalaiselvi, S. Kundu, Iron hydroxyphosphate and Sn-incorporated iron hydroxyphosphate: efficient and stable electrocatalysts for oxygen evolution reaction, *Catal. Sci. Technol.* 7 (21) (2017) 5092–5104, <https://doi.org/10.1039/c7cy00515f>.

[44] Q. Zhang, H. Qi, C. Hou, N. Liu, J. Guan, High-performance Fe–Co–Sn oxide electrocatalysts for oxygen evolution reaction, *Mater. Today Energy* 14 (2019), <https://doi.org/10.1016/j.mtenr.2019.100364>.

[45] Y. Xu, Y. Sheng, M. Wang, T. Ren, K. Shi, Z. Wang, X. Li, L. Wang, H. Wang, Interface coupling induced built-in electric fields boost electrochemical nitrate reduction to ammonia over CuO@MnO₂ core-shell hierarchical nanoarrays, *J. Mater. Chem. A* 10 (32) (2022) 16883–16890, <https://doi.org/10.1039/d2ta02006h>.

[46] Y. Jiang, H. Liu, Y. Jiang, Y. Mao, W. Shen, M. Li, R. He, Adjustable heterointerface-vacancy enhancement effect in RuO₂@Co₃O₄ electrocatalysts for efficient overall water splitting, *Appl. Catal. B Environ.* 324 (2023), <https://doi.org/10.1016/j.apcatb.2022.122294>.

[47] H. Liu, J. Cheng, W. He, Y. Li, J. Mao, X. Zheng, C. Chen, C. Cui, Q. Hao, Interfacial electronic modulation of Ni₃S₂ nanosheet arrays decorated with Au nanoparticles boosts overall water splitting, *Appl. Catal. B Environ.* 304 (2022), <https://doi.org/10.1016/j.apcatb.2021.120935>.

[48] W. He, J. Zhang, S. Dieckhöfer, S. Varhade, A.C. Brix, A. Lielpeterie, S. Seisel, J.R. C. Junqueira, W. Schuhmann, Splicing the active phases of copper/cobalt-based catalysts achieves high-rate tandem electroreduction of nitrate to ammonia, *Nat. Commun.* 13 (1) (2022) 1129, <https://doi.org/10.1038/s41467-022-28728-4>.

[49] Y. Xu, M. Wang, K. Ren, T. Ren, M. Liu, Z. Wang, X. Li, L. Wang, H. Wang, Atomic defects in pothole-rich two-dimensional copper nanoplates triggering enhanced electrocatalytic selective nitrate-to-ammonia transformation, *J. Mater. Chem. A* 9 (30) (2021) 16411–16417, <https://doi.org/10.1039/dita04743d>.

[50] L. Li, C. Tang, X. Cui, Y. Zheng, X. Wang, H. Xu, S. Zhang, T. Shao, K. Davey, S. Z. Qiao, Efficient nitrogen fixation to ammonia through integration of plasma oxidation with electrocatalytic reduction, *Angew. Chem. Int. Ed.* 60 (25) (2021) 14131–14137, <https://doi.org/10.1002/anie.202104394>.

[51] D.P. Butcher, A.A. Gwirth, Nitrate reduction pathways on Cu single crystal surfaces: effect of oxide and Cl⁻, *Nano Energy* 29 (2016) 457–465, <https://doi.org/10.1016/j.nanoen.2016.06.024>.

[52] D. Philip, A. Eapen, G. Aruldhans, Vibrational and surface enhanced Raman scattering spectra of sulfamic acid, *J. Solid State Chem.* 116 (2) (1995) 217–223, <https://doi.org/10.1006/jssc.1995.1206>.

[53] R. Zhao, Q. Yan, L. Yu, T. Yan, X. Zhu, Z. Zhao, L. Liu, J. Xi, A Bi-Co corridor construction effectively improving the selectivity of electrocatalytic nitrate reduction toward ammonia by nearly 100, *Adv. Mater.* 35 (48) (2023), <https://doi.org/10.1002/adma.202306633>.

[54] R. Hao, S. Fang, L. Tian, R. Xia, Q. Guan, L. Jiao, Y. Liu, W. Li, Elucidation of the electrocatalytic activity origin of Fe₃C species and application in the NO_x full conversion to valuable ammonia, *Chem. Eng. J.* 467 (2023), <https://doi.org/10.1016/j.cej.2023.143371>.

[55] J. Liu, B. Cheng, J. Yu, A new understanding of the photocatalytic mechanism of the direct Z-scheme g-C₃N₄/TiO₂ heterostructure, *Phys. Chem. Chem. Phys.* 18 (45) (2016) 31175–31183, <https://doi.org/10.1039/C6CP06147H>.

[56] H. Li, L. Zhou, L. Wang, Y. Liu, J. Lei, J. Zhang, *In situ* growth of TiO₂ nanocrystals on g-C₃N₄ for enhanced photocatalytic performance, *Phys. Chem. Chem. Phys.* 17 (26) (2015) 17406–17412, <https://doi.org/10.1039/C5CP02554K>.

[57] C. Lyu, C. Cao, J. Cheng, Y. Yang, K. Wu, J. Wu, W.-M. Lau, P. Qian, N. Wang, J. Zheng, Interfacial electronic structure modulation of Ni₂P/Ni₅P₄ heterostructure nanosheets for enhanced pH-universal hydrogen evolution reaction performance, *Chem. Eng. J.* 464 (2023) 142538, <https://doi.org/10.1016/j.cej.2023.142538>.